



Cite this: *RSC Adv.*, 2025, **15**, 20668

## Probing the effect of the disordered flank regions on amyloid fibril growth and proliferation<sup>†</sup>

Jacob Aunstrup Larsen, <sup>‡a</sup> Juami H. M. van Gils, <sup>‡b</sup> Soumik Ray, <sup>a</sup> Marcel Dickmanns, <sup>c</sup> Shuangyan Wang, <sup>a</sup> Ahmed Sadek, <sup>d</sup> Hossein Mohammad-Beigi, <sup>a</sup> Masoumeh Zanganeh, <sup>a</sup> Sanne Abeln <sup>\*be</sup> and Alexander K. Buell <sup>\*a</sup>

Amyloid fibrils typically consist of a dense core made up of  $\beta$ -strands, with disordered flanks on either side, and are sometimes interrupted by disordered loop regions (the fuzzy coat).  $\alpha$ -Synuclein found in Lewy Bodies of Parkinson's Disease patients is mostly C-terminally truncated, meaning that a large fraction of the fuzzy coat of disease-related fibrils is enzymatically degraded in the amyloid state. We demonstrate that the proteolytic removal of the fuzzy coat leads to enhanced fibril–fibril interactions and flocculation, which renders the study of the role of the fuzzy coat in bulk solution very challenging. In order to overcome these challenges, here we use Quartz Crystal Microbalance with Dissipation (QCM-D), a surface based biosensing technique, to study the effects of proteolytic removal of the fuzzy coat of  $\alpha$ -synuclein amyloids. We demonstrate that Dissipation-Frequency analysis can illuminate multiple simultaneous reactions and characterize the monomer–fibril interactions in detail. We find that removal of the fuzzy coat increases apparent fibril elongation rates permanently. Utilizing kinetic models, we demonstrate that our results cannot be rationalized by alterations of the elongation rate of fibrils alone, but indicate that proteolytic cleavage of the fuzzy coat of  $\alpha$ -synuclein fibrils can lead to the formation of new growth-competent fibril ends. We propose that such phenomena may be highly relevant for understanding disease-related  $\alpha$ -synuclein amyloid formation. Furthermore we suggest that the QCM-D is a particularly attractive platform for studying post-translational modifications in real-time and their effect on amyloid growth or molecular interactions.

Received 7th March 2025

Accepted 21st May 2025

DOI: 10.1039/d5ra01654a

rsc.li/rsc-advances

## 1 Introduction

$\alpha$ -Synuclein is a protein normally involved in synaptic vesicle transport and exocytosis for neurotransmission.<sup>1–3</sup> Aggregation of  $\alpha$ -synuclein is a primary feature of the synucleinopathies, such as Parkinson's Disease (PD), multiple system atrophy (MSA) and Lewy Body dementia (LBD).<sup>4–7</sup> Neuropathological examination of PD and LBD brains reveals the formation of intra-cellular inclusions called Lewy Bodies (LBs).<sup>4–6,8–10</sup> LBs are spherical structures consisting of aggregated  $\alpha$ -synuclein in an amyloid conformation,<sup>11–14</sup> lipids,

organelles and other proteins, such as cytoskeletal proteins.<sup>8–10</sup> While the pathological importance of LBs has been well known for decades, the mechanism behind their formation remains incompletely understood.<sup>8–10</sup>  $\alpha$ -Synuclein molecules within LBs are mostly post-translationally modified, with ubiquitination, phosphorylation and truncations being particularly prominent.<sup>8–10</sup> C-terminal truncations of  $\alpha$ -synuclein species are expected to occur post fibril formation, demonstrated in neuronal models capable of recreating LB-like inclusions.<sup>8,9</sup> The strongly negatively charged C-terminal region of  $\alpha$ -synuclein is located outside the fibril core of the amyloid conformation<sup>13,14</sup> and constitutes part of the so-called “fuzzy coat”.<sup>15</sup> Within recent years an increasing number of amyloid core structures have been determined at an atomic level by cryo-EM techniques.<sup>16</sup> However, the fuzzy coat is effectively invisible or only available in low resolution to modern imaging techniques due to its highly dynamic and disordered nature.<sup>15,17,18</sup> This means that, in many cases, a large part of the total amino acid sequence, and more than half of the total sequence in the case of  $\alpha$ -synuclein fibrils<sup>19</sup> remains structurally uncharacterized. The fuzzy coat is important for the biophysical properties of amyloid, having significant effects on kinetic parameters<sup>15,17,20–22</sup> and can even govern the mechanical and adhesive properties of amyloid fibrils.<sup>23</sup> The oligomeric assemblies of  $\alpha$ -synuclein, which are

<sup>a</sup>Department of Biotechnology and Biomedicine, Technical University of Denmark, Søltofts Plads, 2800 Lyngby, Denmark. E-mail: s.abeln@uu.nl; alebu@dtu.dk

<sup>b</sup>Bioinformatics Group, Computer Science Department, Vrije Universiteit Amsterdam, de Boelelaan 1111, 1081HV, Amsterdam, The Netherlands

<sup>c</sup>Max Planck Institute of Biochemistry, Am Klopferspitz 18, 82152 Martinsried, Germany

<sup>d</sup>Institute of Bioengineering, École Polytechnique Fédérale de Lausanne (EPFL), Rte Cantonale, 1015 Lausanne, Switzerland

<sup>AI</sup> Technology for Life, AI & Data Science, Utrecht University, Princetonplein 5, 3584CC, Utrecht, The Netherlands

<sup>†</sup> Electronic supplementary information (ESI) available. See DOI: <https://doi.org/10.1039/d5ra01654a>

<sup>‡</sup> These authors contributed equally to the work.



suspected to be the drivers of amyloid neurotoxicity, are indeed also formed by fibril-surface catalyzed pathways.<sup>24</sup> Furthermore the disordered flank regions may control the access of chaperones to the fibril core, such as Hsp70 which is able to depolymerize  $\alpha$ -synuclein amyloid fibrils under ATP consumption.<sup>25</sup>

Increased knowledge of the roles of the fuzzy coat and its implications for amyloid kinetics and cellular interactions would therefore provide an important step towards understanding the role of amyloid in disease as well as identifying new targets for drug development. It is therefore important to establish experimental approaches which allow for systematic investigation of the biophysical properties of the fuzzy coat. Indeed Ulamec and co-workers recently called for the development of assays of protease treated fibrils, with the fuzzy coat “shaven off”, to study which parts of the fibril are driving binding and intracellular interactions.<sup>15</sup>

Here, we demonstrate an approach which allows for the systematic investigation of biophysical properties of amyloid fibrils subjected to protease treatment. We show that classical bulk measurement approaches of protease treated amyloid fibrils are challenging due to flocculation and loss of ThT sensitivity of  $\alpha$ -synuclein fibrils, but surface-based biosensing approaches, such as Quartz Crystal Microbalance with Dissipation (QCM-D), provide suitable experimental platforms for such investigations. We demonstrate that the detailed information provided by the method allows to distinguish molecular interactions such as protein binding/adsorption to the fibrils and fibril growth. We compare the growth rate of  $\alpha$ -synuclein amyloid fibrils with and without the fuzzy coat “shaven off” and propose a consistent molecular model that explains the sustained increase in aggregation rate observed after the proteolytic treatment through enhanced secondary processes.

## 2 Methods

### 2.1 Materials

Proteinase K, from *Tritirachium album*, phenylmethylsulfonyl fluoride (PMSF) and 2-iminothiolane hydrochloride were purchased from Sigma-Aldrich (USA). Poly(ethylene glycol) methyl ether thiol was procured from Polypure AS (NO) and Human-serum Protein was purchased from Biowest (FRAN). QCM-D gold sensors were purchased from Biolin Scientific AB (SE). ZipTip MicroSPE Pipette Tips were obtained from Millipore Corporation (Bedford, MA, USA). Markers: Precision Plus Protein<sup>TM</sup> Standards and Precision Plus Protein<sup>TM</sup> Dual Xtra Standards were purchased from Bio-Rad (USA), while Color Marker Ultra-low Range (M.W. 1060–26 600) was purchased at Sigma-Aldrich (USA).

### 2.2 $\alpha$ -Synuclein WT expression and purification

To obtain  $\alpha$ -synuclein for the experiments, BL21 (DE3) *E. coli* cultures, carrying the pT-7 plasmid encoding the WT human  $\alpha$ -synuclein gene, were grown overnight. The culture was used to inoculate 1 L of LB-Amp medium in a 3 L flask and was grown at 37 °C at 180 rpm shaking. When OD<sub>600</sub> = 0.8 was reached protein expression was induced by adding IPTG to a final concentration of 1 mM. The induced cells were incubated for 4 h at 37 °C at 180 rpm

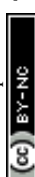
shaking. The cells were harvested by centrifugation at 4 °C, 7000×g for 20 min and stored at -20 °C until further use. Bacterial pellets corresponding to 1 L of culture were resuspended in 20 mL of 10 mM Tris-HCl, 1 mM EDTA, pH 8.0 with 1 mM PMSF. The suspension were sonicated with a probe sonicator for 2 min at 10 s intervals with 30 s pause at 40% amplitude. 1  $\mu$ L benzonase was added to the cell lysate and centrifuged at 4 °C, 20 000×g for 30 min. The supernatant was collected and the solution heated to 80 °C for 20 min. The solution was subsequently centrifuged at 4 °C, 20 000×g for 20 min to precipitate the heat-sensitive proteins,  $\alpha$ -synuclein remaining in the supernatant. Next, 4 mL saturated (NH<sub>4</sub>)<sub>2</sub>SO<sub>4</sub> was added for 1 mL supernatant to salt out  $\alpha$ -synuclein. The solution was stirred at 4 °C for 15 min and centrifuged at 4 °C, 20 000×g for 20 min to pellet down the protein. The pellet was dissolved in 7 mL of 25 mM Tris-HCl pH 7.7 and 7  $\mu$ L DTT added to the final concentration of 1 mM. Next, the protein solution was dialyzed against the same buffer for 16–18 h at 4 °C with a change of the buffer after 12 h of dialysis. The dialyzed protein solution was then subjected to an anion exchange column (AEC) (HiTrap Q Hp 5 mL, GE Healthcare) followed by size exclusion chromatography (SEC) (HiLoad 16/600 Superdex 200 pg, column) and eluted in 10 mM of sodium phosphate buffer (pH 7.4). SEC-chromatogram and SDS-PAGE analysis of the purified protein is shown in Fig. S1.<sup>†</sup> Protein concentrations were assessed by absorption spectroscopy at 280 nm (using a Labbot instrument, Labbot, Lund, Sweden) and the concentrations calculated using theoretical molar extinction coefficients predicted by ProtParam (Expasy, Switzerland).

### 2.3 Expression and purification of 6 $\times$ His-tagged NbSyn2-GFP

**2.3.1 Expression and purification.** The 6 $\times$ His-tagged NbSyn2-GFP chimera was expressed and purified using the same expression and purification approach as described in ref. 26. Briefly, the gene encoding the protein of interest was purchased from Twist Bioscience, cloned into the pHLSec mammalian vector *via* Gibson assembly, and transformed into HB101 *E. coli* for plasmid propagation. Plasmids were extracted using the PureLink Fast Low-Endotoxin Midi plasmid purification kit (Invitrogen, A35892) and verified by Sanger sequencing.

Protein expression was carried out in the Expi293 mammalian expression system (Thermo Fisher, A14635). Six days after plasmid transfection, the supernatant containing the expressed protein was collected, filtered, and purified *via* Ni-NTA affinity chromatography using a HisTrap column, followed by size-exclusion chromatography (SEC) on a Superdex HiLoad 16/600 75 pg column (GE Healthcare). The purified protein was concentrated in PBS, aliquoted and stored at -80 °C until use. The purified protein sequence is as follows:

HHHHHHGSGGSGMVSKGEEELFTGVVPLVELGDVNGHKFSVRGEGEGLDATNGKLTLCFICTTGKLPVPWPTLVTTLTYGVLCFSRYPDHMKRHDFFKSAMPEGYVQERTISFKDDGTYKTRAEVKFEGLTDLVNRIELKGIDFKEDGNILGHKLEYNFSHNVYITADKQKNGIKAYFKIRHNVEDGSVQLADHYQQNTPIGDGPVLLPDNHYLSTQSVLSKDPNEKRDRHMVLLEDVTAAGITHGMDELYKGSGGGSGENLYFQSWGPGGQLVESGGSVQAGGSLRLSCAASGIDSSSYCMGW



FRQRPKEREVARINGLGGVKTAYADSVKDRFTISRDNAENTV  
YLQMNSLKPEDTAIYYCAAKFSPGYCGGSWSNFGYWQGTQVT  
VSSH

Corresponding to the following construct:

HIS-tag — GSGGSG — *mGFP* — GSGGSGENLYFQSWGPG —

### NbSyn2

**2.3.2 Characterization.** Size-exclusion chromatography coupled with multi-angle light scattering (SEC-MALS; mini-DAWN TREOS, Wyatt) was used to determine the molecular weight and the oligomeric state of purified NbSyn2-GFP. The protein sample, at a final concentration of  $\sim 1$  mg mL $^{-1}$  in PBS (pH 7.4), was injected (100  $\mu$ L) onto a Superdex 75 10/300 GL column (GE Healthcare) and eluted at a flow rate of 0.5 mL min $^{-1}$ . Signals for ultraviolet absorbance (280 nm), differential refractive index, and light scattering were recorded. Molecular weight calculations were performed using ASTRA software (v.6.1, Wyatt). Characterization of the purified protein is in Fig. S2.<sup>†</sup>

### 2.4 $\alpha$ -Synuclein fibril preparation

*De novo*  $\alpha$ -synuclein fibrils were prepared by incubating 500  $\mu$ L of 100  $\mu$ M  $\alpha$ -synuclein monomer in 20 mM sodium phosphate buffer with 150 mM NaCl in a 1.5 mL Eppendorf tube that was incubated at 37 °C for 14 days. The solution was shaken at 1200 rpm with a 1 mm diameter glass bead using a ThermoMixer. All subsequent fibril solutions were prepared by seeding fresh monomer solutions with 5% monomer equivalent of the original fibril sample. 500  $\mu$ L of 100  $\mu$ M  $\alpha$ -synuclein monomer, in a 1.5 mL Eppendorf tube was incubated at 37 °C in 20 mM sodium phosphate buffer with 150 mM NaCl for 3 days. The solution was shaken at 1200 rpm with a 1 mm diameter glass bead. In order to prepare the seeds,  $\alpha$ -synuclein fibrils were sonicated for 5 minutes (25 minute cycle, 2 s sonication, 8 s break) on ice using a MS72 probe sonicator at 10% amplitude.

### 2.5 Bulk thioflavin T aggregation kinetics

Bulk aggregation kinetics of  $\alpha$ -synuclein amyloid fibrils were performed in a FLUOstar Omega fluorescence microplate reader (BMG Labtech, Germany). All aggregation experiments were performed in 20 mM sodium phosphate buffer with 150 mM NaCl at pH 7.4. Amyloid aggregation was monitored under quiescent conditions at 25 °C by exciting the sample at 440 nm and recording the emission at 480 nm every 10 minutes.  $\alpha$ -Synuclein amyloid fibrils were grown at 50  $\mu$ M monomer concentration with 5% sonicated amyloid seeds. Aggregation was monitored for two of the six wells by addition of 100  $\mu$ M Thioflavin T (ThT) and fibrils were grown until a plateau was reached. Half the wells were incubated with 200 nM proteinase K (PK) for 30 minutes. 100  $\mu$ M PMSF was added to all wells as a PK inhibitor and incubated overnight. 50  $\mu$ M monomer was added to each well and 100  $\mu$ M ThT to all ThT-free wells and the monitoring of the aggregation reaction was resumed until a plateau in ThT fluorescence is reached.

### 2.6 Capillary flocculation assay

Capillary flocculation assays were performed using square glass capillaries of 0.4 mm inner diameter and walls of 0.2 mm (VitroCom, Mountain Lakes, NJ, USA). Homogenized  $\alpha$ -synuclein amyloid seeds of 25  $\mu$ M equivalent monomer concentration in 20 mM sodium phosphate buffer, 150 mM NaCl and 50 mM ThT, were mixed with 20 nM PK, loaded into a capillary and monitored for 18 h at 5 min intervals. The capillary was imaged using a Zeiss Axio vert. A1 microscope (Zeiss, Germany) with a 10 $\times$  objective lens equipped with a CFP filter cube (model no. 424931, ex. 436/20, beam splitter 455, emission 480/40), illuminated using a Visitron Cool LED pE100 (Visitron Systems, Germany) operating at 440 nm. Flocculation was quantified from relative standard deviation of ThT intensity across the area of the inner capillary.

### 2.7 Quartz crystal microbalance with dissipation experiments

$\alpha$ -Synuclein fibril seeds were immobilized on a QCM-sensor by chemical modification with 2-iminothiolane (Traut's reagent).<sup>27</sup>  $\alpha$ -Synuclein fibrils at 100  $\mu$ M equivalent monomer mass were treated with 2-iminothiolane at 0.15 mg mL $^{-1}$  for 5 minutes prior to being incubated with an UV-ozone activated QCM gold-sensor for 1 h. The sensors were rinsed in buffer and then incubated with 1 vol.% mPEG-thiol in buffer for 30 min. Sensors were rinsed with miliQ water and dried prior to being inserted into the instrument. All treatment of fibrils in the QCM instrument were performed at 20 mM sodium phosphate buffer with 150 mM NaCl.

We measured the elongation of amyloid fibrils by injecting 3 cell volumes (60  $\mu$ L) of monomeric protein solutions at 50  $\mu$ M in 20 mM sodium phosphate buffer with 150 mM NaCl and 1 mM PMSF into different sensor chambers and monitored the third overtone frequency. PMSF was added to ensure that residual active PK was inhibited. PMSF was added to the  $\alpha$ -synuclein solutions from a 0.2 M stock dissolved in ethanol, leaving a residual volume fraction of 0.5% ethanol. Fibril "shaving" was achieved by injecting 3 cell volumes of 20 nM PK and subsequent incubation. Proteinase was washed out by flushing the cell with at least 20 cell volumes of buffer. To inhibit remaining proteinase, 3 cell volumes of 5 mM PMSF were injected then and incubated for at least 10 minutes. The cell was then flushed with at least 20 cell volumes of buffer.

Human serum Protein (HsP) binding experiments were performed by injecting 3 cell volumes of 1% HsP solution into the sensor chamber and monitoring the third overtone frequency. Fibril elongation experiments in complex medium were measured by injecting 3 cell volumes of 1% HsP + 50  $\mu$ M  $\alpha$ -synuclein into the sensor chamber and monitoring the third overtone frequency.

NbSyn2-GFP binding experiments were performed by injecting 3 cell volumes of 5  $\mu$ M protein in PBS buffer into the sensor chamber and monitoring the third overtone frequency. Fibrils were treated with PK and subsequently PMSF treated in accordance with above.



## 2.8 Characterization of $\alpha$ -synuclein fibril modification by PK

200  $\mu$ L  $\alpha$ -synuclein fibrils at 50  $\mu$ M equivalent monomer concentration were split into two. One sample was incubated with 200 nM PK for 30 minutes. Both samples were subsequently centrifuged at 16 900 RCF for 30 minutes to form fibril pellets. The supernatant was removed and the fibrils were re-suspended in 20 mM sodium phosphate buffer with 150 mM NaCl and 5 mM PMSF. This washing process was repeated three times so as to remove any active PK. The fibrils were pelleted again and re-suspended in 100  $\mu$ L 8 M urea with 5 mM PMSF and sonicated using a Vial Tweeter powered by an ultrasonic processor UP200St (200 W, 26 kHz; Hielscher Ultrasonic, Teltow, Germany). The samples were sonicated for 10 minutes using a 2 s *on* to 8 s *off* scheme. The samples were then incubated for three days to depolymerize before being buffer exchanged to 20 mM sodium phosphate buffer with 150 mM NaCl and 5 mM PMSF using a Amicon Ultra Centrifugal Filter, 3 kDa MWCO.

Samples were desalted prior to Matrix-Assisted Laser Desorption Ionization Time of Flight (MALDI-TOF) analysis using C18 ZipTip, employing the protocol provided by the supplier. Samples were analyzed on an Ultraflex II MALDI-TOF/TOF mass spectrometer (Bruker). Samples were prepared for spotting by mixing 0.5  $\mu$ L of sample with 0.5  $\mu$ L of  $\alpha$ -cyano-4-hydroxy-trans-cinnamic acid (saturated solution in 70% acetonitrile, 0.1% TFA). The spectrum was calibrated using peptide standard II (Bruker).

Samples were prepared for SDS-PAGE by mixing with NuPAGE<sup>TM</sup> LDS Sample Buffer and heated to 90 °C for 10 minutes. SDS-PAGE was run using NuPAGE<sup>TM</sup> Bis-Tris Mini Protein Gels, 4–12%, 1.0 mm and NuPAGE<sup>TM</sup> MES SDS Running Buffer, running at 200 V for 40 min. The gel was stained by Coomassie blue dye overnight (InstantStain<sup>TM</sup> 15 Min, MinKem-En-Tec Nordic A/S) and destained by deionized water wash for 24 hours.

## 2.9 Kinetic models

Five kinetic models were created to model the QCM-D results, assuming different monomer–fibril interactions. The null model (Model 0), describes amyloid fibril elongation of non-modified fibrils. Model A is the simplest model, which describes amyloid fibril elongation without the repulsive charges of the fuzzy coat. No surface binding or secondary nucleation takes place in this model. In addition to elongation, Model B also allows monomers to bind to the surface when no disordered flanks are present. In Model C, surface binding enables secondary nucleation and subsequent growth. After every PK degradation step new nucleation viable binding sites become available. Model D assumes that protofilaments can be proteolytically fragmented by PK degradation, leading to the generation of new growth-competent fibril ends. Formal descriptions of the models are provided in the SI.

# 3 Results

## 3.1 Flocculation of shaven fibrils inhibits growth in bulk

In order to investigate the significance of the fuzzy coat (disordered flanks) on the kinetic parameters of  $\alpha$ -synuclein amyloid

growth, we performed bulk ThT aggregation experiments. We grew fibrils both in the presence of ThT and without, to identify if the fibril–ThT interaction was modified by PK treatment. We grew fibrils until a plateau was obtained in ThT-containing samples in quiescent conditions to maximize fibril length. This maximizes the ratio of surface area to the number of ends, prior to protease treatment. We then introduced PK in half the wells, to “shave” the fuzzy coat of the fibrils. PK is subsequently inhibited by the addition of PMSF to all wells. After “shaving” with PK and subsequent inhibition of the PK, we add fresh monomer to all wells and ThT to wells, where ThT was absent in the initial growth step. Growth rates after the addition of fresh monomer are similar for all samples, however the increase in ThT fluorescence intensity of shaven fibrils ceases rather abruptly, and the ThT fluorescence decreases afterwards (Fig. 1A). In order to investigate whether the observed apparent cessation of fibril growth stems from a genuine decrease of the elongation rate constant, decreased ThT sensitivity or rather from increased higher order assembly of shaven fibrils, we compared the colloidal behavior of unmodified and shaven fibrils in a microscopic capillary assay. The fibrils were subjected to probe sonication right before the measurement, in order to start from a homogeneous fluorescence and therefore fibril distribution, whereby no granularity of the fluorescence signal was observed with our microscope.

We find that the ThT intensity of the shaven fibrils decreases by over 50% within the shaving phase (100 min). Additionally we find that the shaven fibrils are more prone to higher order assembly (flocculation) than non-shaven fibrils, inducing larger spatial variability in ThT intensity across the micro capillary, compared to the sample without PK treatment (Fig. 1B). We quantify the degree of flocculation through the spatial standard deviation of fluorescence intensity of the entire field of view of the capillary. This higher order assembly is likely to affect the accessibility of the fibril ends for monomer. The strong tendency of shaven  $\alpha$ -synuclein fibrils to undergo higher order assembly is unsurprising, given the highly negatively charged and disordered C-terminal tail is removed, which otherwise provides electrostatic and steric repulsion of other molecules. It is reasonable to assume that removal of the fuzzy coat not only affects the higher order assembly of fibrils and interactions with small molecules, such as ThT, but surface interactions with the monomeric protein as well, as charges are removed and the hydrophobic core becomes more accessible. These various effects conspire to render a quantitative comparison of the intrinsic elongation rates of intact and shaven fibrils in such bulk solution assays very challenging. In addition, we cannot fully exclude residual activity of the inhibited PK in such a bulk solution assay.

## 3.2 PK incubation degrades the majority of the fuzzy coat

In order to characterize the extend of degradation of the fuzzy coat, we depolymerized both untreated and shaven fibrils by chemical denaturation. The released monomers, were subsequently investigated by both SDS-PAGE and MALDI-TOF (Fig. S3†). The SDS-PAGE analysis reveals that the released



monomers of the shaven fibrils are a uniform species, characterized by a single band. The band corresponds to approximately  $9.9 \pm 0.3$  kDa, whereas the released monomer from untreated fibrils are the same size as the monomer control –  $14.4 \pm 0.3$  kDa. The MALDI-TOF spectrum of the released monomer from shaven fibrils shows peaks at 5.5, 8.1 and 11.7 kDa. The difference between SDS-PAGE and MALDI-TOF analysis can be explained by the differential sensitivity and resolution of these two methods for molecular species of different size and charge. The MALDI-TOF peak intensities at 5.5 and 8.1 kDa are relatively low and these species may not be visible on the gel. The monomer control reveals a species of approximately 14.5 kDa, as expected. In the absence of a high resolution structure, it is difficult to ascertain precisely what fraction of the fuzzy coat is susceptible to being removed. However, similar solution conditions have generally revealed that the structured core is composed of residues 33–97 (PDB: 6a6b). Assuming the fibrils generated here are structurally similar, we can estimate the degree of fuzzy coat degradation as:

$$\frac{MW_{\alpha\text{Syn}} - MW_{\text{shaven}}}{MW_{\alpha\text{Syn}} - MW_{33-97}} = \frac{14.46 - 9.9 \text{ kDa}}{14.46 - 6.17 \text{ kDa}} = 55\% \quad (1)$$

The same calculations show the MALDI-TOF peaks correspond to 100%, 76% and 33% fuzzy coat degradations respectively.

### 3.3 QCM-D reveals accelerated growth following PK incubation

In order to investigate the elongation behavior of shaven  $\alpha$ -synuclein fibrils without complications from fibril flocculation and altered ThT-sensitivity, we employed QCM-D measurements. The QCM-D instrument is sensitive to attachment of mass to the sensor surface, where the addition of mass decreases the sensor oscillation frequency ( $\Delta F$ ). Changes in structure and material properties of the surface-bound layer, such as viscoelasticity, can be inferred from changes in energy dissipation to the environment ( $\Delta D$ ). To characterize amyloid elongation, we monitored multiple recurring growth phases of  $\alpha$ -synuclein fibrils immobilized on a QCM-D sensor (Fig. 2A–C). Upon injection a rapid change in frequency and dissipation is observed. This effect originates from the viscosity and density change of solution, as the  $\alpha$ -synuclein solution contains 0.5 v/v% ethanol (from addition of the PK inhibitor PMSF, see Methods). Such a water–ethanol mixture is expected to have an

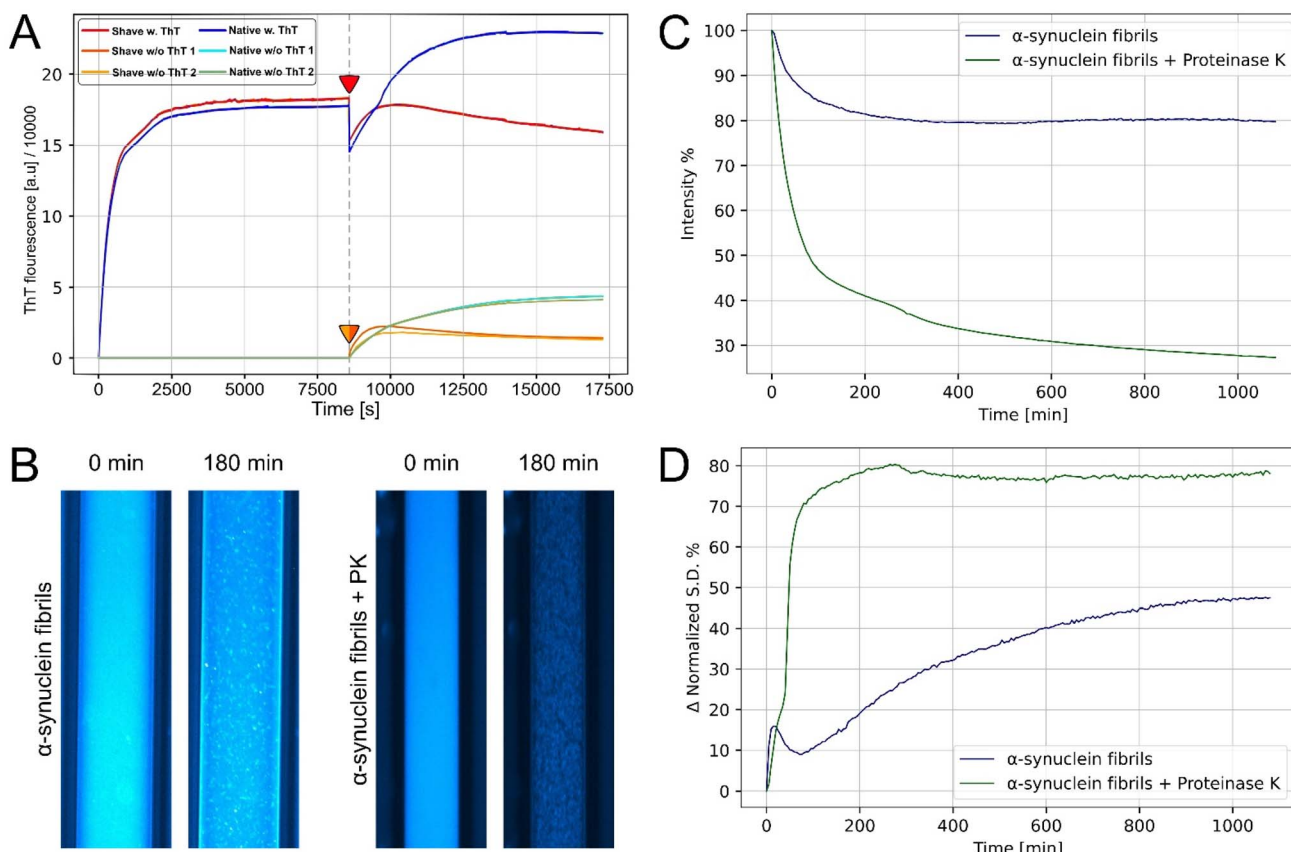
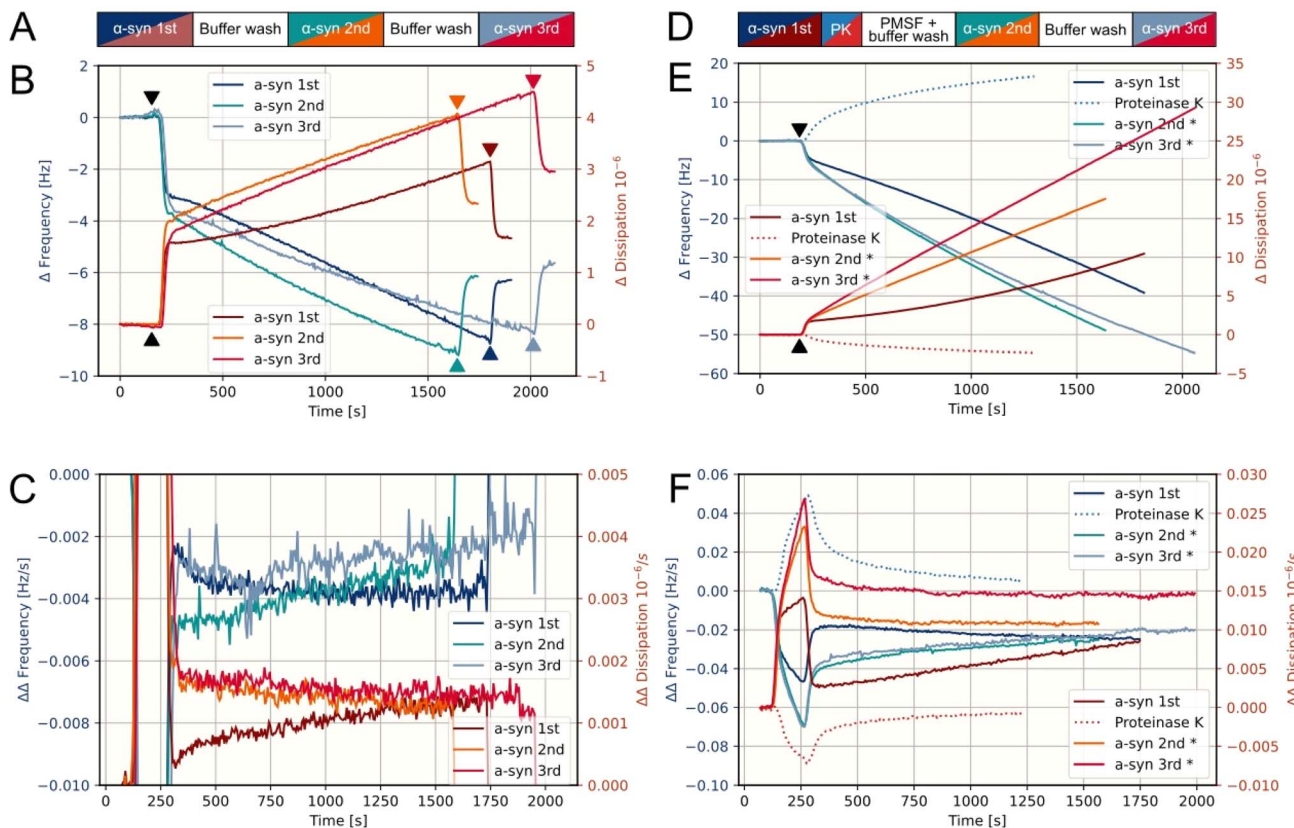


Fig. 1 Time course of ThT fibril growth assay and capillary flocculation assay from ESI Video 1 and 2.† (A) ThT fluorescence of amyloid fibril growth with and without PK. The dashed line indicates addition of monomer to all samples. PK treatment is noted by color-coded arrows. PK is both added and inhibited before the addition of fresh monomer outside the plate-reader instrument. However, the treatment time, where no data is gathered, is not shown in this graph. ThT is added to samples labeled "w/o ThT" along with additional monomer. Numbering indicates technical repeats. (B) Sample images of capillaries from ESI Video 1 and 2† at time 0 and 180 min. (C) Normalized intensity of ThT-fluorescence throughout the experiment. (D) Change in relative spatial standard deviation of ThT-fluorescence intensity across the capillary as a function of time.





**Fig. 2** QCM-D analysis of  $\alpha$ -synuclein fibrils and PK exposure, showing the 3rd overtone. All QCM-D traces represent individual measurements. (A) Flow-scheme for B. Each  $\alpha$ -synuclein injection is color-coded to the respective frequency and dissipation legend-colors in B. (B) Frequency and dissipation change of three subsequent growth phases of  $\alpha$ -synuclein fibrils on the same sensor. Black arrows indicate the injection time of each solution as labeled in the legends. Color-coded arrows indicate the start of buffer rinse. The initial rapid change of frequency and dissipation upon injection is reversible and is caused by viscosity and density differences in the solutions. (C) Slope of frequency and dissipation change (i.e. growth rate) of B. (D) Flow-scheme for E.  $\alpha$ -synuclein and PK injections are color-coded to the respective frequency and dissipation legend-colors in E. (E) Frequency and dissipation change of three growth phases of  $\alpha$ -synuclein fibrils on the same sensor and a single PK degradation phase, between the first and second growth phase. Stars mark the total number of shaving phases prior to the injection. (F) Slope of frequency and dissipation change (i.e. growth rate) of E.

approximately 10% higher viscosity than pure water.<sup>28</sup> The viscosity-induced shift in frequency and dissipation is reversible when returning to pure buffer conditions (Fig. 2B). During periods of incubation with monomer solution, the frequency and dissipation change linearly in time, demonstrating that both dissipation and frequency changes report on fibril growth. Amyloid growth rates are expected to be constant throughout each growth phase, as monomer is not significantly depleted in the cell within the time of the measurements at the monomer concentrations employed.<sup>29</sup> However, during the last growth phase the rate of the frequency response decreases throughout the measurement, while the rate of dissipation change remains constant. This behaviour can be explained by fibrils growing beyond their persistence length<sup>30</sup> and increasingly extend away from the sensor surface into the solution where the mass sensitivity decreases. The dissipation response appears to be less affected by this phenomenon compared to the frequency response.

In order to investigate the effect of the fuzzy coat using the QCM-D, we must demonstrate that surface-immobilized fibrils

are “shaven” similar to fibrils in solution. To this end we have studied binding of a nanobody (a NbSyn2-GFP construct). NbSyn2 binds to residues 137–140 and has been demonstrated to be unable to bind to C-terminally truncated  $\alpha$ -synuclein fibrils.<sup>31</sup> We incubated untreated and shaven fibrils with NbSyn2 and find that PK incubation of  $\alpha$ -synuclein fibrils indeed abolishes the nanobody binding (Fig. 3A), suggesting that the majority of accessible C terminal ends are degraded by PK-incubation. Therefore, we conclude that the effect of PK on the fibrils does not differ significantly between fibrils suspended in solution or immobilized on a QCM-D sensor.

To investigate the effect of the fuzzy coat on fibril growth, we utilized an experimental scheme of a single standardized growth phase prior to a shaving step followed by two subsequent growth phases (Fig. 2D). In all growth phases we inject full length WT  $\alpha$ -synuclein. During fibril shaving we observe a fast release of mass, which decays as the PK-degradable material, the fuzzy coat, is removed and becomes increasingly unavailable. The frequency response during monomer incubation, post shaving, is approximately 80% accelerated by

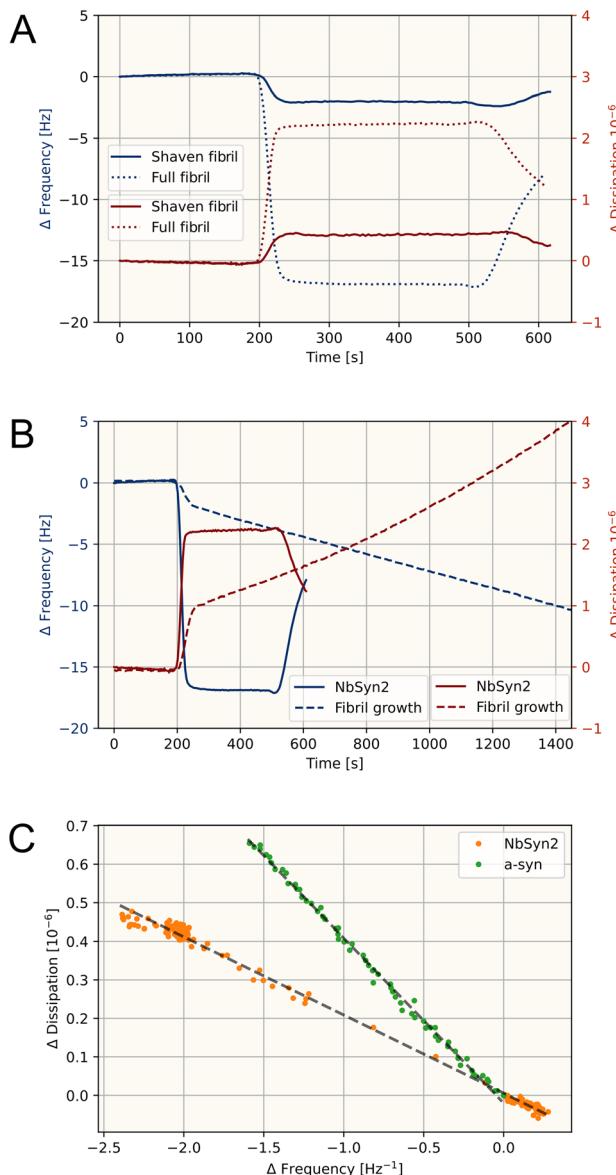


Fig. 3 QCM-D analysis of NbSyn2 binding to amyloid fibrils, showing the 3rd overtone. All QCM-D traces represent an individual measurement. (A) NbSyn2 binding to shaven fibrils (solid) and untreated fibrils (dotted) when exposed to solutions at time 200 s. (B) NbSyn2 binding to untreated fibrils (solid) and fibril growth by incubation with  $\alpha$ -synuclein (dashed) when exposed to solutions at time 200 s. (C) DF-plot of data from B, with linear fits in black dashes. The slope of NbSyn2 binding is  $-0.20$ , while the slope of amyloid fibril growth is  $-0.43$ .

frequency and 35% by dissipation and demonstrates the same slow decrease in frequency response as the growth experiments of intact fibrils. This behavior occurs in both post shaving growth phases, however in the last growth phase the dissipation response is accelerated by 80%. It is not immediately obvious whether the accelerated deposition of mass to the sensor surface originates from monomer binding to the exposed fibril core or accelerated fibril elongation. However, the dissipation response is constant throughout the majority of the measurement, suggesting that the signal is dominated by fibril growth

rather than monomer binding, which would be expected to saturate as the shaved fibril surface becomes increasingly covered. In addition, the ratio of dissipation to frequency response during the growth phases is greater than what we find during the shaving phase (approximately  $-0.3 \times 10^{-6}/\text{Hz}$  and  $-0.15 \times 10^{-6}/\text{Hz}$  respectively), indicating that the material properties of the removed mass by PK treatment is different from the predominant mass contribution during monomer addition post-shaving. It is reasonable to expect that the material properties of monomer attached to the shaven fibril surface would be more similar to those of the fuzzy coat than to those of the fibril core. These results therefore suggest that monomer binding is not contributing significantly to the response of incubation with monomer post shaving.

### 3.4 QCM-D can discriminate between fibril growth and protein binding

To characterize the origin of the accelerated growth following fibril shaving, we must elucidate if binding of protein to the fibril surface can be distinguished from amyloid elongation. To this end, we studied the characteristic QCM-D responses from fibril growth and protein binding or adsorption. Plotting  $\Delta D$  versus  $\Delta F$  is commonly used to obtain structural information of adsorbed molecules, classically referred to as a DF plot.<sup>32,33</sup> When we plot amyloid fibril growth and NbSyn2 binding in such a manner, we obtain significantly different slopes, showing twice the dissipation response of fibril growth compared to binding (Fig. 3B and C). This would suggest that protein binding to fibril surfaces distinctly differs from fibril growth in regards to material properties, and fibril growth and protein binding to fibril surfaces can be distinguished in a single measurement.

To further demonstrate this, we exposed  $\alpha$ -synuclein amyloid fibrils to 1% Human Serum Protein (HsP) that binds to the fibrils causing a decrease in frequency of  $-12$  Hz, while the dissipation increases only  $0.3 \cdot 10^{-6}$  giving a distinctly different response from fibril growth (Fig. 4A, the HsP binding is not non-specific binding to the sensor surface, see Fig. S4†). As a result, when fibrils are exposed to a solution with both 1% HsP and 50  $\mu\text{M}$   $\alpha$ -synuclein, fibril growth can be monitored through the dissipation response, which remains constant throughout the measurement. Meanwhile, the frequency response has contributions from both protein (HsP) binding to the fibrils as well as fibril growth.

The DF plot demonstrates that HsP binding is characterized by a single phase, while fibril growth features two phases (viscosity induced frequency and dissipation change—the injection phase—and fibril growth) and the mixture of HsP and  $\alpha$ -synuclein shows three distinct phases (the injection phase, a HsP binding dominated phase and a fibril growth dominated-phase). The fibril growth-dominated phase is characterized by a linear relationship between  $\Delta D$  and  $\Delta F$ . The  $\Delta D$ - $\Delta F$  slope in both conditions are similar ( $-0.20 \cdot 10^{-6}/\text{Hz} \pm 0.001$  for pure  $\alpha$ -synuclein and  $-0.21 \cdot 10^{-6}/\text{Hz} \pm 0.0003$  for  $\alpha$ -synuclein + HsP), showing that the measurement is dominated by the same type of material deposition in these phases. Employing this linear



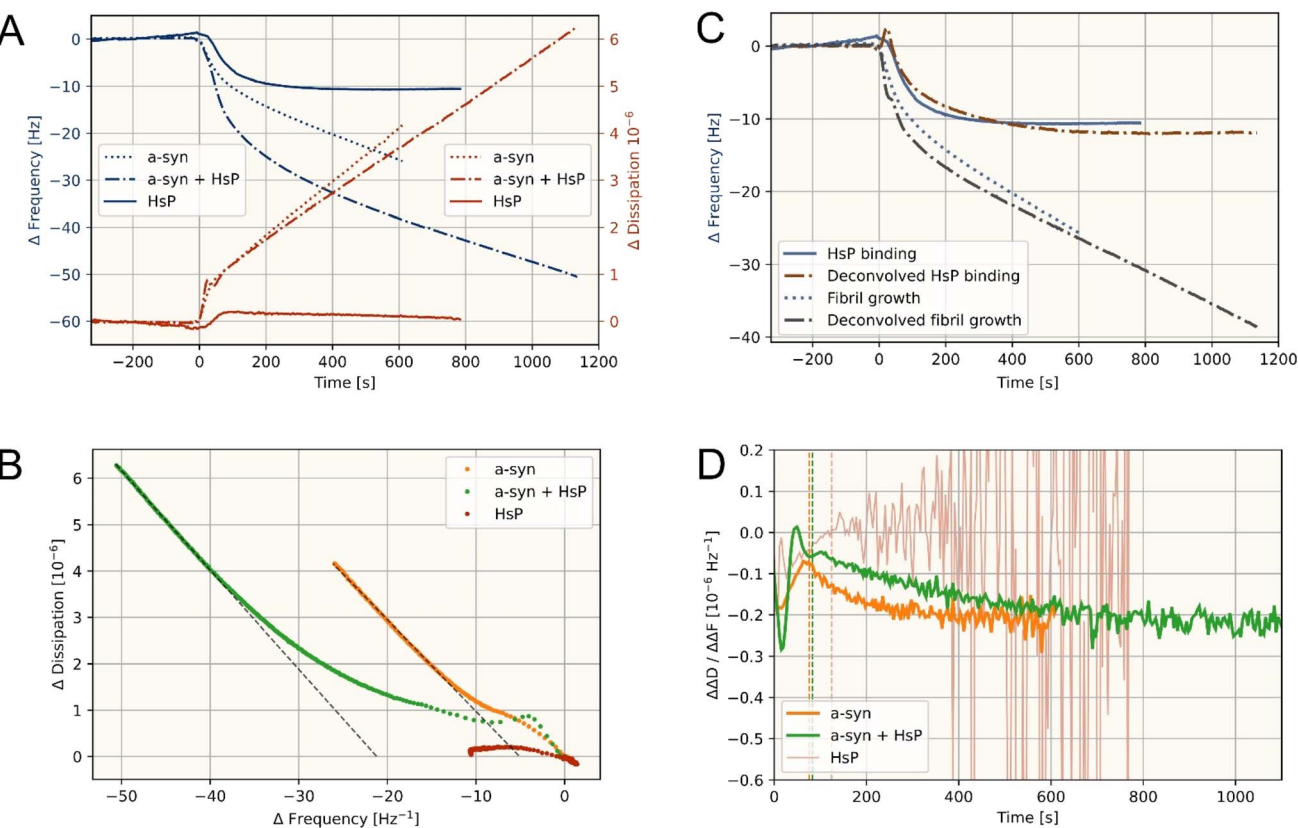


Fig. 4 QCM-D analysis of  $\alpha$ -synuclein growth and binding with HsP, showing the 3rd overtone. All QCM-D traces represent individual measurements. (A) Frequency and dissipation change of QCM-D sensors with immobilized  $\alpha$ -synuclein fibrils when exposed to solutions at time 0. Pure  $\alpha$ -synuclein and pure HsP are measured on the same sensor in that order. (B) DF plot of data from A. Linear fits to the data of fibril growth are shown as dashed lines. (C) De-convoluted HsP binding and fibril growth of the " $\alpha$ -synuclein + HsP" sample in A. The pure fibril growth and HsP binding samples from A are plotted for comparison using the same line-styles as in A. The deconvoluted fibril growth response is obtained by converting the dissipation response in A to a frequency response, using the DF slope fitted in B. The deconvoluted HsP binding is obtained by subtracting the deconvoluted fibril growth response from the raw data. (D) Time-resolved DF plot obtained from numerical derivatives of A. Dashed lines note when the pump is shut off.

relationship, we can disentangle the HsP binding and fibril growth signals (Fig. 4C). As such we can conclude that the dissipation response of the HsP +  $\alpha$ -synuclein incubation, which is constant throughout the entire measurement, reports almost exclusively on the addition of fibrillar material. The  $\Delta D / \Delta F$  relationship can be plotted in the time-domain from the numerical derivatives, which provides insight into the duration of each of the phases. From this analysis we find that the pure  $\alpha$ -synuclein incubation reports solely on fibril growth approx. 200 s after the start of the injection of the monomer solution. The HsP +  $\alpha$ -synuclein converges to pure fibril growth after 5 minutes of incubation.

By comparing the different overtones, we find a frequency overtone dependency of the fibril growth response, while no such dependency is present for HsP binding (Fig. S6†). This finding suggests that a large contribution to the frequency shift during fibril growth originates from liquid contributions, whereas the HsP binding frequency response is dominated by the dry mass,<sup>34</sup> consistent with the  $\Delta D$  to  $\Delta F$  ratio of each mechanism. Our observations agree with earlier findings that the QCM frequency response can be attributed in large parts to water trapped in the fibril matrix.<sup>29</sup>

To demonstrate that  $\alpha$ -synuclein monomer binding can be discerned during fibril growth, we have measured amyloid elongation of  $\alpha$ -synuclein at pH 5.5, where the protein is close to its isoelectric point and surface binding of monomer can be expected, as secondary nucleation is strongly enhanced under these conditions.<sup>35,36</sup> While no clear bi-phasic behavior is evident in the raw data, the DF-plot reveals a low  $\Delta D$  to  $\Delta F$  phase in the early time steps of the pH 5.5 growth phase, which becomes exacerbated after PK treatment (Fig. S7†). The time-resolved DF-plots show a lower dissipation response during the first 200 seconds of the incubation period before the DF-response converges to the signature of amyloid elongation. Compared to injections at pH 7.4, where the elongation signature is achieved within 1 minute of incubation, it is therefore clear from the DF-plots that some non-fibrillar mass deposition occurs, likely monomer attachment to the fibril surface (Fig. S7†).

### 3.5 Proteinase K treatment increases the number of fibril ends

By employing the above described approach we can demonstrate that the material properties of the growth signal following



PK incubation, as indicated by the QCM-D signal, are similar to that of the intact fibrils (Fig. S8†) and show that the material deposited to the surface is mostly fibrillar in nature in all growth phases. We find no indication that monomer binding accounts for a significant fraction of the deposited material in any of the measurements as the DF response is effectively continuous between each growth phase (ignoring the short injection phases). Furthermore, we find that the frequency dependence on overtones are comparable between the shaven and non-shaven fibrils, further demonstrating that the nature of the deposited material is similar between the samples (Fig. S9†).

To further understand the role of the fibril surface in the observed behavior and the nature of the PK modification, we studied fibrils grown over extensive incubation periods. We employed a single standardization growth step followed by several shaving and growth steps, incubating the fibrils for 15 hours with monomer per shaving step (Fig. 5A). Post shaving, the long fibrils demonstrate a significantly enhanced elongation rate sustained increasingly as the fibrils have grown. During the final growth phase the accelerated growth is sustained for over 10 hours. DF analysis of the growth phases reveals that, while some structural reorganization of the fibril matrix may occur in the early time points of the growth phases, the dominant source of added mass originates from amyloid fibril elongation (Fig. 5D). It is notable that the accelerated growth rate is additive, suggesting that the source of accelerated growth must be the fibril surface, rather than any structural modification of the fibril ends.

Each shaving step, *i.e.* incubation with PK, is maintained until a constant low rate of frequency increase is reached, thereby ensuring that the accessible disordered regions are mostly degraded. The remaining release of mass at low constant rate is likely to originate from fibril shortening from the ends, where the accessibility of the fibril core to PK is highest. By investigating the DF plots of PK incubations, we find that the  $\Delta D$  to  $\Delta F$  relationship of the shaving phase converges towards a dissipation insensitive reaction, as the fibrils are grown for longer periods of time prior to shaving (Fig. 5G). This is consistent with the observation that PK treatment predominantly removes non-core material, which does not significantly contribute to dissipation, but also slowly shortens the fibrils from the end. For longer fibrils, the PK treatment is increasingly dominated by the removal of non-core material as the surface-to-end ratio is increased. We find a linear relationship between the frequency response of mass added through fibril elongation and the frequency response of the shaving reaction (Fig. 5H) in agreement with removal of the entire available fuzzy coat and fibril shortening not significantly contributing to the degradation response. The shaven material corresponds to  $16.2 \pm 2.7\%$  of the frequency response of the grown fibrils. This, however, does not mean that the PK necessarily degrades 16% of the fibril, which would only correspond to approximately 30% of the fuzzy coat (PDB 6a6b). The frequency response of fibril growth has a significant liquid contribution, which is demonstrated by the high  $\Delta D$  to  $\Delta F$  ratio and overtone dependency. However, this is not the case for the shaven material, which has a low  $\Delta D$  to  $\Delta F$  ratio and no significant overtone

divergence (Fig. S10†). If the liquid contribution of the full fibril accounts for at least 50% of the frequency response, it follows that the PK treatment removes at least 56% of the fuzzy coat – consistent with the findings in solution:

$$\frac{|f_{\text{coat}}|}{|f_{\text{dryfib}}| + |f_{\text{liq.fib}}|} = 0.16 \quad (2)$$

$$|f_{\text{dryfib}}| \leq |f_{\text{liq.fib}}| \rightarrow \frac{|f_{\text{coat}}|}{|f_{\text{dryfib}}|} \leq 0.32 \quad (3)$$

$$\frac{0.32}{1 - \text{MW}_{33-97}/\text{MW}_{\alpha\text{Syn}}} = 56\% \quad (4)$$

In summary, we find little evidence of binding of monomeric protein to the fibril surfaces contributing significantly to the mass deposition in any experiment at pH 7.4, a cumulative acceleration of growth rates with each shaving step, as well as a linear correlation between the shaven mass and accumulated fibril surface. The observed accelerated fibril growth can thus only be rationalized by the formation of new growth-competent fibril ends on the sensor surface.

### 3.6 Kinetic models show that the increase in growth rate can be explained by partial proteolytic fibril fragmentation

To further investigate the fibril growth, as measured by QCM-D, we constructed kinetic models of the frequency response to fibril growth and modification by several different molecular level scenarios (Fig. 6). The models make different assumptions on the nature of interactions between the full length monomers and amyloid fibrils (shaven and unshaven), and how those interactions translate into changes in growth rate. The null model (Model 0) describes elongation of non-modified amyloid fibrils, assuming that the growth rate of fibrils is conserved between different growth periods. Model A is the simplest model, which includes amyloid fibril elongation without the repulsive charges of the fuzzy coat. The growth rate is accelerated following the removal of the fuzzy coat, but rapidly returns to baseline as the recruited full length monomer reintroduces charges to the fibril ends. Model B extends model A by allowing monomers to bind to the surface of shaven fibrils. Monomer binding leads to an acute increase in surface-associated mass (on a similar timescale to NbSyn2 binding to intact  $\alpha$ -synuclein fibrils—Fig. 3), and an initial increase in apparent fibril elongation rates. In Model C, surface binding enables secondary nucleation and subsequent growth on the shaven fibril surface. After every PK degradation step new nucleation-viable binding sites become available, resulting in a sustained increase in growth rate in subsequent growth phases. Notably, fibril growth accelerates throughout the growth phase, as new fibrils nucleate. Model D assumes that protofilaments can be proteolytically fragmented by PK degradation leading to an increase in the number of fibril ends during the shaving period as the newly accessible proto-filament ends are capable of recruiting monomers.



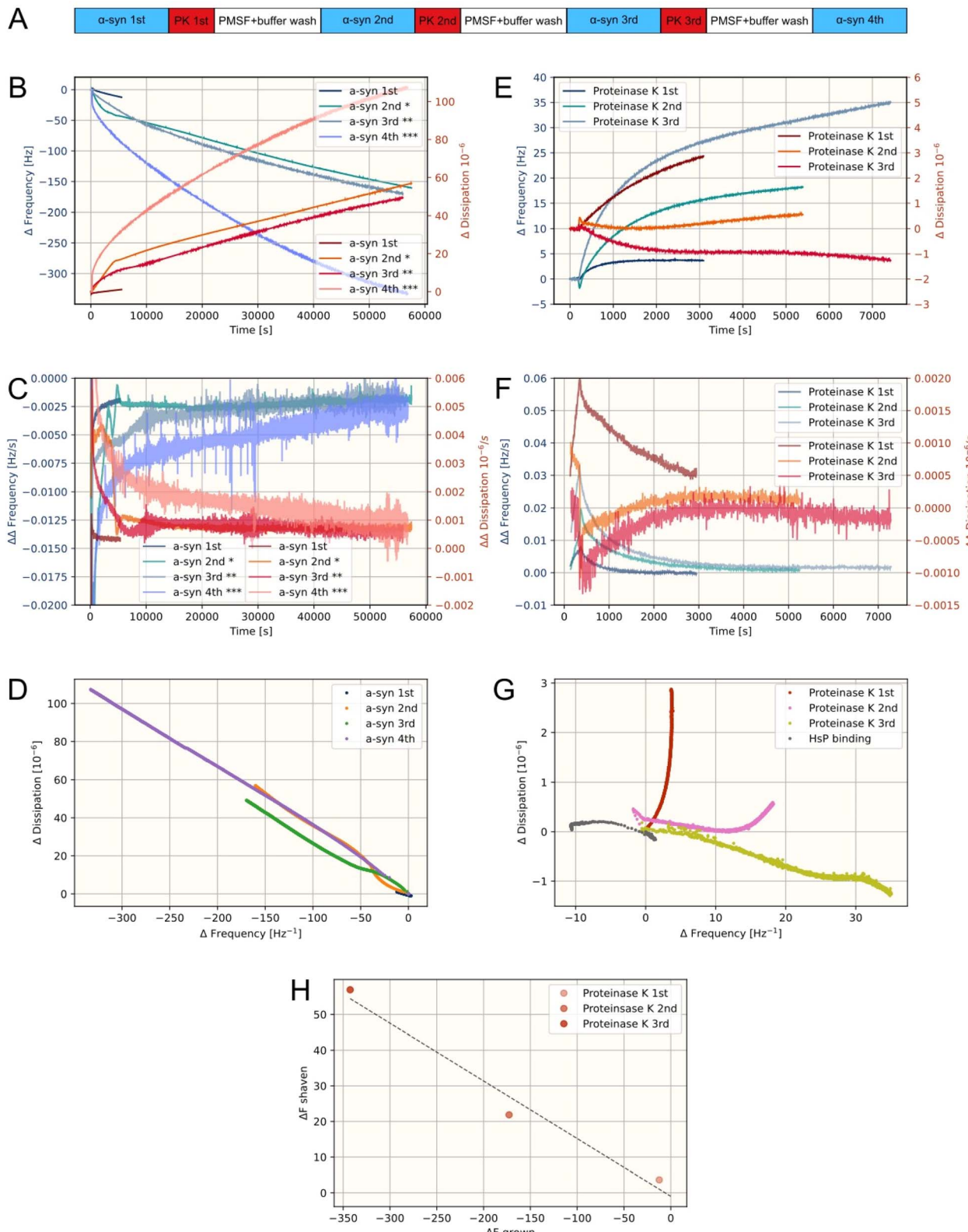


**Fig. 5** QCM-D analysis of amyloid fibril growth for extended time-intervals (+500 min) with shaving steps prior to incubation periods beyond the initial normalization period. The 3rd overtone is shown here. All QCM-D traces represent individual measurements. (A) Flow-scheme used for the measurement. (B) Frequency and dissipation change for all  $\alpha$ -synuclein growth phases. Stars mark the total number of shaving phases prior to the injection. (C) Slope of frequency and dissipation change (i.e. growth rate) of B. (D) DF-plot of data from B. (E) Frequency and dissipation change for all PK degradation phases. (F) Slope of frequency and dissipation change (i.e. growth rate) of E. (G) DF-plot of data from E and HsP binding data from Fig. 4B. (H) Accumulated frequency shift during PK degradation phases plotted against accumulated frequency shift during prior growth phases.

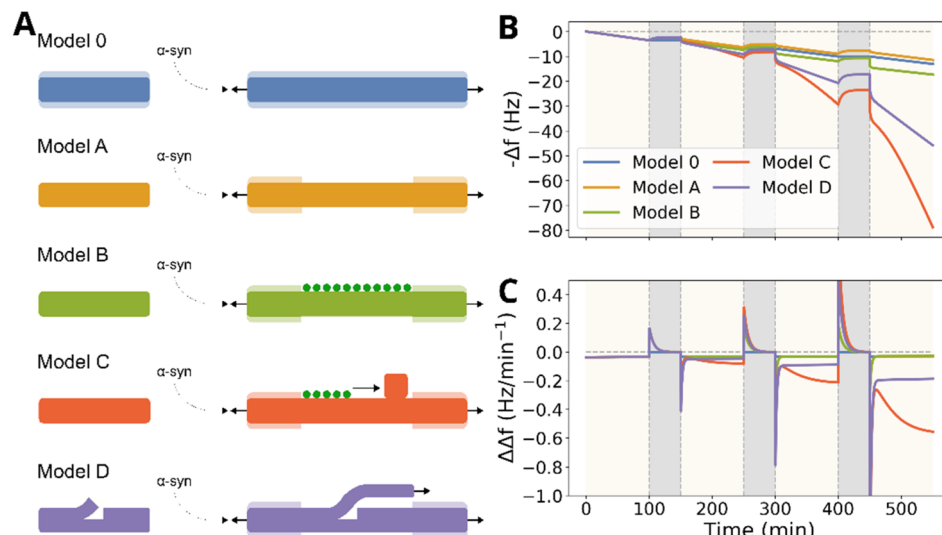


**Fig. 6** Kinetic models showing the expected growth rates in QCM-D experiments for different scenarios of amyloid fibril aggregation. (A) Different models. Model 0: fibril elongation with disordered flanks. Model A: fibril elongation without flanks and surface binding of  $\alpha$ -synuclein. Model B: fibril elongation without flanks and branched growth of new fibrils off the surface. Model C: Fibrils may get broken up by PK during the shaving phase, which creates additional fibril ends. (B) Expected frequency changes corresponding to amyloid fibril growth and shaving phases for the different models. Note that the absolute values on the y-axis are not expected to correspond to the same values as found in experiments, as they depend on the initial surface concentration of fibrils. (C) Expected slopes of B.

The null model captures the qualitative behaviour of fibril growth without any shaving phases (Fig. 2A and 6B). Both models A and B predict increased rates of mass addition only for very short periods of time, which is not what we observe in our experiments. Rather the accelerated growth rates are maintained for many hours. Accelerated mass association to the sensor surface for times extending beyond tens of minutes are only expected in the kinetic models, where the formation of new fibril ends occurs (Model C and D). Model C demonstrates accelerating growth rates throughout the growth phases, whereas our measurements demonstrate constant or decelerating growth rates throughout a single growth phase. Finally, only model D captures the immediate acceleration in fibril growth rates after PK treatment, which is observed in our experiments, suggesting that the additional fibril ends are made available during the PK degradation phase.

## 4 Discussion

In this work, we have studied the growth behavior of proteinase K-treated  $\alpha$ -synuclein amyloid fibrils. Using bulk solution measurements we demonstrate several challenges with biochemical analysis of PK-treated fibrils by traditional methods. Shaven fibrils demonstrate low colloidal stability resulting in extensive flocculation. Furthermore, shaving of the fibrils strongly alters their ThT sensitivity. QCM-D has been demonstrated to be a well adapted label-free methodology for the study of amyloid fibril growth and has been employed for this purpose for over fifteen years.<sup>30</sup> Here we demonstrate that QCM-D can discriminate between protein binding to the fibril surface and fibril elongation, using several protein systems. This enables not only measurements of fibril elongation rates in

complex media, as demonstrated here for Hsp/ $\alpha$ -synuclein mixtures, but provides detailed insights into the nature of deposited material. Utilizing this experimental platform we demonstrate that shaven fibrils are fully capable of recruiting intact monomer.

It has been speculated that intrinsically disordered sequence regions can facilitate molecular interactions and recognition through dynamically sampling a large spatial region and therefore increasing the probability of encounter, a process dubbed fly-casting.<sup>17</sup> In the case of  $\alpha$ -synuclein, it has been proposed that monomers are recruited to the fibril end through interactions with the fuzzy-coat.<sup>37,38</sup> Our finding that removal of the fuzzy coat does not inhibit nor decrease the elongation rate of fibrils indicates that the fuzzy coat of  $\alpha$ -synuclein fibrils does not play a significant role in recruitment of monomers to the fibril end under the conditions of our experiments.

The highly negatively charged C-terminal regions and slightly positively charged N-terminal regions of  $\alpha$ -synuclein fibrils are suspected to decorate the fibril surface as a polymer brush.<sup>39,40</sup> The grafting of charged polymer brushes to colloids increases their colloidal stability against association.<sup>41</sup> It has been shown that the higher order association of  $\alpha$ -synuclein amyloid fibrils strongly depends on pH and ionic strength.<sup>35</sup> Furthermore, electrostatic and steric repulsion between the fibril surface and monomer at neutral pH are suspected to largely prevent monomer-dependent secondary nucleation on the fibril surface.<sup>35,36</sup> Upon shaving of the fibrils, repulsion between fibrils decreases, which results in a decrease in colloidal stability as demonstrated here. The electrostatic and steric repulsion between the fibril surface and monomer should also decrease. However, we find that the primary signal related to mass deposition at pH 7.4 originates from fibril elongation,



independently of the presence of the fuzzy coat, suggesting that monomer binding is inhibited even without the presence of the polymer brush. It may be the case that the residual fuzzy coat still acts as a sufficient polymer brush to inhibit the monomer interaction at neutral pH, since the presented protocol only removes approximately half of the fuzzy coat—which would also leave approximately half of the surface-accessible charges remaining. However, we find that at pH 5.5—close to the isoelectric point and where secondary nucleation has been demonstrated to play an important role<sup>35,36</sup>—removal of the fuzzy coat indeed leads to increased monomer binding, suggesting that the polymer brush effect of the fuzzy coat is decreased upon shaving. Combined, this may suggest that monomeric protein binding to the fibril surface, at neutral pH, is limited by electrostatic repulsion between the monomers themselves, rather than by properties of the fibril surface.

In this work we demonstrate that proteolytic treatment of  $\alpha$ -synuclein fibrils can increase the apparent growth rate in an additive manner. We demonstrate by kinetic modelling, that these observations can only be rationalized by the formation of new fibril ends. Since the QCM-D instrument is a surface-based biosensor, the detected mass can only originate from material anchored to the surface. Hence, any secondary fibrils must adhere to the surface of the sensor in order to be detected. As the sensor surface itself has been passivated with a self-assembled monolayer of PEG, the newly formed fibril ends are likely to adhere to the surfaces of the initial population of seed fibrils. It follows that secondary fibrils detected here must effectively be anchored to the hydrophobic core of the shaved fibrils by non-covalent forces without detaching. This observation is similar to findings in A $\beta$ 42, where daughter fibrils formed through secondary nucleation have been observed to adhere to the fibril surface for extended periods of time.<sup>42</sup>

However, in these measurements, we do not observe continued acceleration of mass addition rates to the sensor surface during long incubation periods with monomer solutions post-shaving. Instead we find a sudden increase in growth rates following each shaving step. If the increase in the number of growing fibril ends were caused by monomer-dependent secondary nucleation, new fibril ends should constantly be formed during incubation with monomer and therefore an acceleration, rather than a slowing down of mass deposition would be expected—as observed over long incubation periods (Fig. 5C and 6C). It appears that new fibril ends are only created during the incubation with PK. Thus, the experimental results combined with the kinetic models suggest that the proteolytic modification of fibrils itself can act as a source of secondary growth sites. Monomer-dependent secondary nucleation of  $\alpha$ -synuclein is strongly enhanced at mildly acidic pH,<sup>35–37</sup> presumably restraining exponential amplification of fibrils by secondary nucleation to environments such as endosomes and lysosomes.<sup>43</sup> However, our findings, that secondary fibril ends may originate from proteolytic modification of  $\alpha$ -synuclein fibrils even at neutral pH, suggests an alternative pathway for amyloid amplification in the cellular environment.

It is intriguing to speculate that changes in cohesive properties of  $\alpha$ -synuclein fibrils upon proteolytic truncation of the

fuzzy coat, such as colloidal stability and formation of strongly adhering secondary daughter fibrils, may play an important role in disease and formation of LBs. Flocculation and higher order assembly of fibrils and further growth by elongation and secondary pathways could indeed form structures similar to LBs, with a dense core and radiating filaments.<sup>8</sup> However, our study does not investigate if LB-like structures form from these conditions. It may be the case that the fuzzy-coat generally could inhibit and slow down the aggregation of proteins<sup>44</sup> and formation of toxic inclusion bodies, and hence be an evolved protective feature.

The QCM-D platform proves to be particularly useful for studying amyloid fibrils. By demonstrating the ability to discern protein-fibril interactions and fibril growth in a quantitative manner, we enable detailed studies of fibrils in more complicated chemical environments than have been previously performed on the platform. In addition, since the instrument is based on a flow cell setup, fibril modifications can be monitored and terminated effectively in real time, enabling detailed control of fibril modifications. By not relying on reporter-molecules, such as fluorescent dyes, the instrument provides a reliable response to growth or binding of molecules to modified fibrils, where changes in ThT sensitivity can otherwise be an experimental barrier. The QCM-D platform is, therefore, advantageous for studying relative binding affinities to species commonly found in LBs, such as lipids and other proteins. Systematic study of PTMs and fibril binding affinities may allow for a bottom-up approach to the study of LB formation, not easily available through other experimental *in vitro* platforms.

## 5 Conclusion

In summary, we have illustrated that the surface-based bio-sensing technique QCM-D can provide insights into amyloid growth mechanisms of modified fibrils which may be unavailable in bulk measurements due to flocculation, changes in dye sensitivity and persistent modifying agents. We demonstrate that dissipation-frequency (DF)-plots allow the discrimination of addition/removal of mass originating from fibril core and noncore regions as well as surface binding of proteins. Combining our QCM-D results with kinetic modelling, we show that proteolytic truncation of the disordered flanking regions of fibrils does not abolish their ability to elongate through the addition of unmodified monomer. Furthermore, such proteolysis leads to the generation of additional growth-competent ends at neutral pH, where monomer-dependent secondary nucleation is otherwise inefficient, and hence suggests the existence of a new secondary pathway with potential relevance for the proliferation of amyloid pathology *in vivo*.

## Data availability

The authors declare that the data supporting the findings of this study are available within the main text or the ESI.<sup>†</sup> All figure data and analysis code are available at the Zenodo repository at <https://doi.org/10.5281/zenodo.14136660> and will be published upon paper acceptance.

## Author contributions

JL and JvG performed QCM-D experiments on fibril growth. JL, HMB and MZ performed HsP binding QCM-D experiments. JL performed NbSyn2-GFP binding experiments. JL and MD performed capillary fluorescence assays. SR and JL performed the ThT bulk experiments. JL and SW performed characterization experiments of PK-modified fibrils. AS generated and characterized the NbSyn2-GFP construct. AKB, SA and JvG were responsible for conceptualisation. JvG and SA created the kinetic models. JL, JvG, AKB and SA wrote the manuscript. SA and AKB supervised the project and were responsible for funding acquisition. All authors reviewed the manuscript.

## Conflicts of interest

There are no conflicts to declare.

## Acknowledgements

JvG and SA thank the Nederlandse Organisatie voor Wetenschappelijk Onderzoek (NWO) (<https://www.nwo.nl/over-nwo/organisatie/nwo-onderdelen/enw>) for funding under project number 680-91-112. AKB, HMB and MZ thank the Lundbeck Foundation for funding (R366-2021-169 STADIC). JL, SYW and AKB thank the Novo Nordisk Foundation (grant numbers: NNF17SA0028392, NNF21OC0065495 SEEDFOOD) for funding. SR would like to acknowledge a Horizon MSCA individual postdoctoral fellowship for funding (grant no: 101062241). This research was also funded by the European Union (ERC CoG 101088163 EMMA). Views and opinions expressed are however those of the author(s) only and do not necessarily reflect those of the European Union or the European Research Council. We thank Sandrine Georgeon and Joseph Schmidt for their support with NbSyn2 purification and characterization (Institute of Bioengineering, École Polytechnique Fédérale de Lausanne (EPFL), Lausanne, Switzerland). We thank Louise K. Klausen for their support with  $\alpha$ -synuclein purification and characterization (Department of Biotechnology and Biomedicine, Technical University of Denmark, Søltofts Plads, 2800 Lyngby, Denmark).

## Notes and references

- 1 J. Burré, M. Sharma, T. Tsetsenis, V. Buchman, M. R. Etherton and T. C. Südhof, *Science*, 2010, **329**, 1663–1667.
- 2 T. Logan, J. Bendor, C. Toupin, K. Thorn and R. H. Edwards, *Nat. Neurosci.*, 2017, **20**, 681–689.
- 3 C.-C. Huang, T.-Y. Chiu, T.-Y. Lee, H.-J. Hsieh, C.-C. Lin and L.-S. Kao, *J. Cell Sci.*, 2018, **131**, 1–12.
- 4 C. Peng, R. J. Gathagan and V. M. Lee, *Neurobiol. Dis.*, 2018, **109**, 209–218.
- 5 M. Goedert, R. Jakes and M. G. Spillantini, *J. Parkinsons Dis.*, 2017, **7**, 53–71.
- 6 M. G. Spillantini, R. A. Crowther, R. Jakes, M. Hasegawa and M. Goedert, *Neurobiology Communicated*, ed. M. F. Perutz, Medical Research Council, 1998, vol. 95, pp. 6469–6473.
- 7 E. M. Rocha, B. De Miranda and L. H. Sanders, *Neurobiol. Dis.*, 2018, **109**, 249–257.
- 8 A.-L. Mahul-Mellier, J. Burtscher, N. Maharjan, L. Weerens, M. Croisier, F. Kuttler, M. Leleu, G. W. Knott and H. A. Lashuel, *Proc. Natl. Acad. Sci. U. S. A.*, 2020, **117**, 4971–4982.
- 9 M. B. Fares, S. Jagannath and H. A. Lashuel, *Nat. Rev. Neurosci.*, 2021, **22**, 111–131.
- 10 K. Prasad, T. G. Beach, J. Hedreen and E. K. Richfield, *Brain Pathol.*, 2012, **22**, 811–825.
- 11 K. Araki, N. Yagi, K. Aoyama, C. J. Choong, H. Hayakawa, H. Fujimura, Y. Nagai, Y. Goto and H. Mochizuki, *Proc. Natl. Acad. Sci. U. S. A.*, 2019, **116**, 17963–17969.
- 12 B. Frieg, J. A. Geraets, T. Strohäker, C. Dienemann, P. Mavroeidi, B. V. Jung, W. S. Kim, S. J. Lee, M. Xilouri, M. Zweckstetter and G. F. Schröder, *Commun. Biol.*, 2022, **5**, 1040.
- 13 Y. Yang, Y. Shi, M. Schweighauser, X. Zhang, A. Kotecha, A. G. Murzin, H. J. Gorringer, P. W. Cullinane, Y. Saito, T. Foroud, T. T. Warner, K. Hasegawa, T. Lashley, S. H. Scheres and M. Goedert, *Nature*, 2022, **610**, 791–795.
- 14 T. Strohäker, B. C. Jung, S. H. Liou, C. O. Fernandez, D. Riedel, S. Becker, G. M. Halliday, M. Bennati, W. S. Kim, S. J. Lee and M. Zweckstetter, *Nat. Commun.*, 2019, **10**, 5535.
- 15 S. M. Ulamec, D. J. Brockwell and S. E. Radford, *Front. Neurosci.*, 2020, **14**, 611285.
- 16 S. Lövestam and S. H. Scheres, *Faraday Discuss.*, 2022, **240**, 243–260.
- 17 P. Tompa, *FEBS J.*, 2009, **276**, 5406–5415.
- 18 Z. F. Brotzakis, T. Löhr, S. Truong, S. Hoff, M. Bonomi and M. Vendruscolo, *Biochemistry*, 2023, **62**, 2407–2416.
- 19 A. A. Bhopatkar and R. Kayed, *J. Biol. Chem.*, 2023, **299**, 105122.
- 20 F. Longhena, G. Faustini, C. Missale, M. Pizzi, P. Spano and A. Bellucci, *Neural Plast.*, 2017, **2017**, 5012129.
- 21 I. M. van der Wateren, T. P. J. Knowles, A. K. Buell, C. M. Dobson and C. Galvagnion, *Chem. Sci.*, 2018, **9**, 5506–5516.
- 22 X. Yang, J. K. Williams, R. Yan, M. M. Mouradian and J. Baum, *Sci. Rep.*, 2019, **9**, 17579.
- 23 S. Wegmann, I. D. Medalsy, E. Mandelkow and D. J. Müller, *Proc. Natl. Acad. Sci. U. S. A.*, 2012, **110**, E313–E321.
- 24 C. K. Xu, G. Meisl, E. Andrzejewska, G. Krainer, A. J. Dear, M. C. Cruz, S. Turi, R. Jacquat, W. E. Arter, M. Vendruscolo, S. Linse and T. P. J. Knowles, *bioRxiv*, preprint, 2023, 1–17, DOI: [10.1101/2023.05.28.542651](https://doi.org/10.1101/2023.05.28.542651).
- 25 X. Gao, M. Carroni, C. Nussbaum-Krammer, A. Mogk, N. B. Nillegoda, A. Szlachcic, D. L. Guilbride, H. R. Saibil, M. P. Mayer and B. Bukau, *Mol. Cell*, 2015, **59**, 781–793.
- 26 A. Marchand, S. Buckley, A. Schneuing, M. Pacesa, M. Elia, P. Gainza, E. Elizarova, R. M. Neeser, P.-W. Lee, L. Reymond, Y. Miao, L. Scheller, S. Georgeon, J. Schmidt, P. Schwaller, S. J. Maerk, M. Bronstein and B. E. Correia, *Nature*, 2025, **639**, 522–531.



27 A. K. Buell, D. A. White, C. Meier, M. E. Welland, T. P. Knowles and C. M. Dobson, *J. Phys. Chem. B*, 2010, **114**, 10925–10938.

28 Y. Tanaka, T. Yamamoto, Y. Satomi, H. Kubota and T. Makita, *Rev. Phys. Chem. Jpn.*, 1977, **47**, 12–24.

29 T. C. Michaels, A. K. Buell, E. M. Terentjev and T. P. Knowles, *J. Phys. Chem. Lett.*, 2014, **5**, 695–699.

30 T. P. J. Knowles, W. Shu, G. L. Devlin, S. Meehan, S. Auer, C. M. Dobson and M. E. Welland, *Proc. Natl. Acad. Sci. U. S. A.*, 2007, **104**, 10016–10021.

31 T. Guilliams, F. El-Turk, A. K. Buell, E. M. O'Day, F. A. Aprile, E. K. Esbjörner, M. Vendruscolo, N. Cremades, E. Pardon, L. Wyns, M. E. Welland, J. Steyaert, J. Christodoulou, C. M. Dobson and E. De Genst, *J. Mol. Biol.*, 2013, **425**, 2397–2411.

32 P. Komorek, E. Martin and B. Jachimska, *Int. J. Mol. Sci.*, 2021, **22**, 1–17.

33 F. Höök, M. Rodahl, B. Kasemo and P. Brzezinski, *Proc. Natl. Acad. Sci. U. S. A.*, 1998, **95**, 12271–12276.

34 A. Armanious, B. Agnarsson, A. Lundgren, V. P. Zhdanov and F. Höök, *J. Phys. Chem. C*, 2021, **125**, 1932–7447.

35 A. K. Buell, C. Galvagnion, R. Gaspar, E. Sparr, M. Vendruscolo, T. P. Knowles, S. Linse and C. M. Dobson, *Proc. Natl. Acad. Sci. U. S. A.*, 2014, **111**, 7671–7676.

36 R. Gaspar, G. Meisl, A. K. Buell, L. Young, C. F. Kaminski, T. P. J. Knowles, E. Sparr and S. Linse, *Q. Rev. Biophys.*, 2017, **50**, e6.

37 P. Kumari, D. Ghosh, A. Vanas, Y. Fleischmann, T. Wiegand, G. Jeschke, R. Riek and C. Eichmann, *Proc. Natl. Acad. Sci. U. S. A.*, 2021, **118**, 1–8.

38 X. Yang, B. Wang, C. L. Hoop, J. K. Williams and J. Baum, *Proc. Natl. Acad. Sci. USA*, 2021, **118**, e2017452118.

39 R. Gaspar, M. Lund, E. Sparr and S. Linse, *QRB Discov.*, 2020, **1**, e2.

40 K. K. Sweers, K. O. V. D. Werf, M. L. Bennink and V. Subramaniam, *ACS Nano*, 2012, **6**, 5952–5960.

41 C. M. Wijmans, F. A. Leermakers and G. J. Fleer, *J. Colloid Interface Sci.*, 1994, **167**, 124–134.

42 D. Thacker, M. Barghouth, M. Bless, E. Zhang and S. Linse, *Proc. Natl. Acad. Sci. U. S. A.*, 2023, **120**, 1–9.

43 P. Gracia, J. D. Camino, L. Volpicelli-Daley and N. Cremades, *Int. J. Mol. Sci.*, 2020, **21**, 1–27.

44 S. Abeln and D. Frenkel, *PLoS Comput. Biol.*, 2008, **4**, e1000241.

